10.1002/cssc.202301327

WILEY VCH

RESEARCH ARTICLE

High-performance Ni-free sustainable cathode $Na_{0.67}Mg_{0.05}Fe_{0.1}Mn_{0.85}O_2$ for sodium-ion batteries

Pedro Lavela*, Julia Leyva, José Luis Tirado

Prof. Pedro Lavela*, Julia Leyva, Prof. José Luis Tirado

Departamento de Química Inorgánica e Ingeniería Química. Instituto Químico para la Energía y el Medioambiente (IQUEMA). Universidad de Córdoba. Edificio Marie Curie. Campus de Rabanales 14071 Córdoba (Spain)

Supporting information for this article is given via a link at the end of the document.

Abstract: Having in mind the remarkable economic and environmental issues involved in the presence of nickel and cobalt metals in electrode compositions, new $Na_{0.67}Mg_{0.05}Fe_{0.1}Ni_xMn_{0.85-x}O_2$ (x= 0.0, 0.05, 0.1, 0.15) with a P2 type layered structure, are synthesized to be essayed as positive electrodes in sodium-ion batteries. The sol-gel route here proposed favors the obtention of highly pure and crystalline samples with a homogeneous distribution of the constituting elements. Both galvanostatic and voltammetric tests reveal a superior electrochemical behavior for the Ni-free sample, which delivers 94 mA h g^{-1} at 5C. This excellent performance is associated with a good kinetic response in terms of low charge and discharge hysteresis, high Na^+ diffusivity, and low cell resistance. Ex-situ measurements evidenced the combined contribution of both the reversible electrolyte insertion and the formation of peroxo species. These advantageous properties allow this electrode to reach a remarkable behavior when is cycled either to low temperatures or high rates.

Introduction

Sodium-ion batteries (SIBs) are envisaged as promising electrochemical devices that may compete with lithium-ion batteries (LIBs) for specific niches of applicability.[1-3] Despite certain limitations of Na^+ ions, such as their larger size and slightly reduced power, the vast differences in lithium and sodium carbonate prices and the replacement of copper by aluminum as the anode collectors lead to an effective decrease in battery cost. It can be crucial shortly when the high demand for LIBs or the occurrence of supply constraints could lead to a prohibitive increase in the battery cost.[4-5] For this reason, SIBs are not being fully discarded for specific applications such as the storage of electricity coming from renewable energy sources in which large-scale energy systems would be needed.[6-8]

The search for new electrode materials for SIBs promoting sodium insertion strongly resides in the preliminary successful results reported for LIBs in previous decades. Thus, the literature about anode and cathode materials is abundant.[9, 16] Among others, P2 type $Na_{0.67}Ni_{0.33}Mn_{0.67}O_2$ features an open framework that facilitates the Na^+ ion diffusivity allowing it to reach excellent specific capacities, high ion diffusion coefficients, and cycling stability.[11-20] Despite these benefits, this electrode material suffers from some detriments such as the appearance of an irreversible O2 phase at high voltage and undesirable ordering of Na^+ ions and vacant limiting its applicability.[21] Fortunately, partial replacement of Ni^{2+} by Mg^{2+} has been revealed to be an adequate solution to this issue.[22-24]

Otherwise, the presence of nickel in the nominal composition of this cathode material reveals issues about the safety of supplies that are already concerning for LIBs. McKinsey and Company forecasted that the supply of battery-grade nickel may not meet demands shortly. Moreover, geological scarcity and low incentive prices have been responsible for a decline in the supply of Class 1.[25-27] Likely, the investment required to explore new deposits of sulfide ores to meet the demand for battery-grade nickel will increase the price of this metal. Nickel recovery is an environmentally friendly alternative option able to preserve resources, but it should be considered that the high purity (99%) of Class 1 metal is highly demanding when establishing efficient recycling processes.[28]

Based on these assumptions, the research on new cathodes for SIBs should make an effort to develop new low-Ni content chemistries. Excellent reports on Ni-free layered oxides can be found in the literature.[29-31] Notwithstanding, it is widely admitted that the presence of Ni^{4+}/Ni^{2+} redox couple near four volts is a positive contribution to the energy density of the cell that cannot be discarded.[32, 33] The goal of this work is to unveil whether the presence of nickel is significant to obtaining highly performing cathodes for SIBs.

For the first time, we studied Mg-doped layered oxides with the nominal composition $Na_{0.67}Mg_{0.05}Fe_{0.1}Ni_xMn_{0.85-x}O_2$ ($0 \le x \le 0.15$). Samples were prepared by a single and easily scalable sol-gel method and the morphological and structural properties were characterized by X-ray diffraction, electron microscopy, and spectroscopic techniques. The optimal stoichiometry for achieving between low-Ni content and high electrochemical performance as cathodes for sodium-ion batteries was evaluated by both galvanostatic and potentiostatic methods.

Results and Discussion

The P2 type structure of this sodium layered oxides is the result of the parallel stacking of two-dimensional slabs built from (Mn, Ni, Fe, Mg)O_6 octahedra sharing edges. Sodium ions are

located at partially filled prismatic sites in the interslab space which facilitates their diffusion.[34, 35] The XRD patterns of the studied samples feature a set of narrow reflections which were indexed in the *P6₃/mmc* space group of the hexagonal system (Figure 1). Despite the major presence of the P2 phase, minor reflections at ca. 13º and 25º (2θ) additionally appeared, mainly for NMFN05. It has been ascribed to the occurrence of hydrated phases at low Na content.[36] However, this phase will not involve a significant hindrance to the electrochemical behavior, as will be evidenced below. Table 1 shows that the lattice parameters increase with the Ni content, as expected from the larger crystal radius of Ni^{2+} (0.83 Å) as compared to high-spin Mn^{3+} (0.785 Å) or Mn^{4+} (0.67 Å). X-ray fluorescence evidenced a close similarity between the nominal and actual stoichiometry. The contents of Na, Mg, and Fe were quite similar, while Ni and Mn followed the expected trend (Table 2).

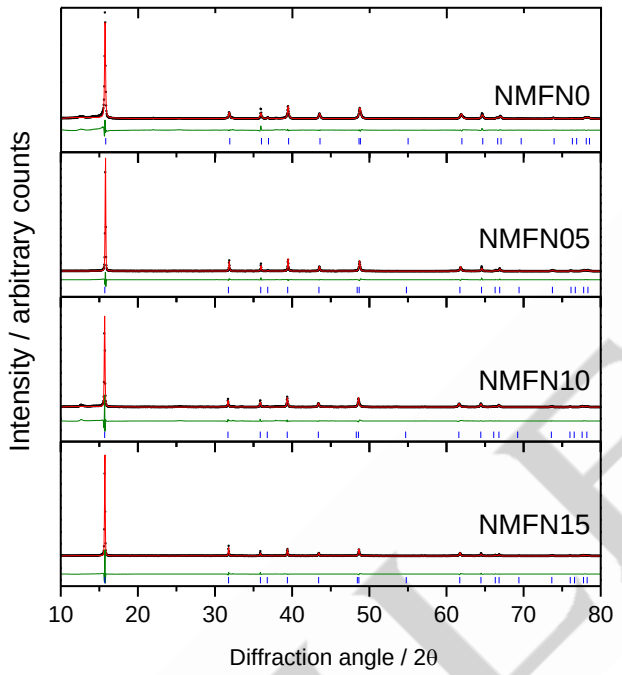

Figure 1. X-ray diffraction patterns of $Na_{0.67}Mg_{0.05}Fe_{0.1}Ni_xMn_{0.85-x}O_2$ ($0 \le x \le 0.15$) series. The experimental patterns (black dots), calculated patterns (red), and differential curves (green) are included for each sample. DIF patterns for the P2-type structure (blue) are displayed.

	NMFN0	NMFN05	NMFN10	NMFN15
a / Å	2.8805(5)	2.8854(2)	2.8880(2)	2.8889(3)
c / Å	11.224(2)	11.258(1)	11.277(1)	11.281(1)
Volume / Å^3	80.65(3)	81.33(1)	81.45(1)	81.53(2)

Table 1 Unit cell parameters for the $Na_{0.67}Mg_{0.05}Fe_{0.1}Ni_xMn_{0.85-x}O_2$ series indexed in the *P6₃/mmc* space group.

Table 2. Nominal and actual stoichiometry determined by XRF for the $Na_{0.67}Mg_{0.05}Fe_{0.1}Ni_xMn_{0.85-x}O_2$ series.

Sample	Nominal stoichiometry	Actual stoichiometry from XRF
NMFN0	$Na_{0.67}Mg_{0.05}Fe_{0.1}Ni_{0.0}Mn_{0.85}O_2$	$Na_{0.67}Mg_{0.05}Fe_{0.11}Ni_{0.0}Mn_{0.96}O_{1.88}$
NMFN05	$Na_{0.67}Mg_{0.05}Fe_{0.1}Ni_{0.05}Mn_{0.8}O_2$	$Na_{0.64}Mg_{0.04}Fe_{0.10}Ni_{0.05}Mn_{0.86}O_{1.96}$
NMFN10	$Na_{0.67}Mg_{0.05}Fe_{0.1}Ni_{0.1}Mn_{0.75}O_2$	$Na_{0.67}Mg_{0.05}Fe_{0.11}Ni_{0.11}Mn_{0.84}O_{1.9}$
NMFN15	$Na_{0.67}Mg_{0.05}Fe_{0.1}Ni_{0.15}Mn_{0.7}O_2$	$Na_{0.68}Mg_{0.05}Fe_{0.11}Ni_{0.17}Mn_{0.83}O_{1.84}$

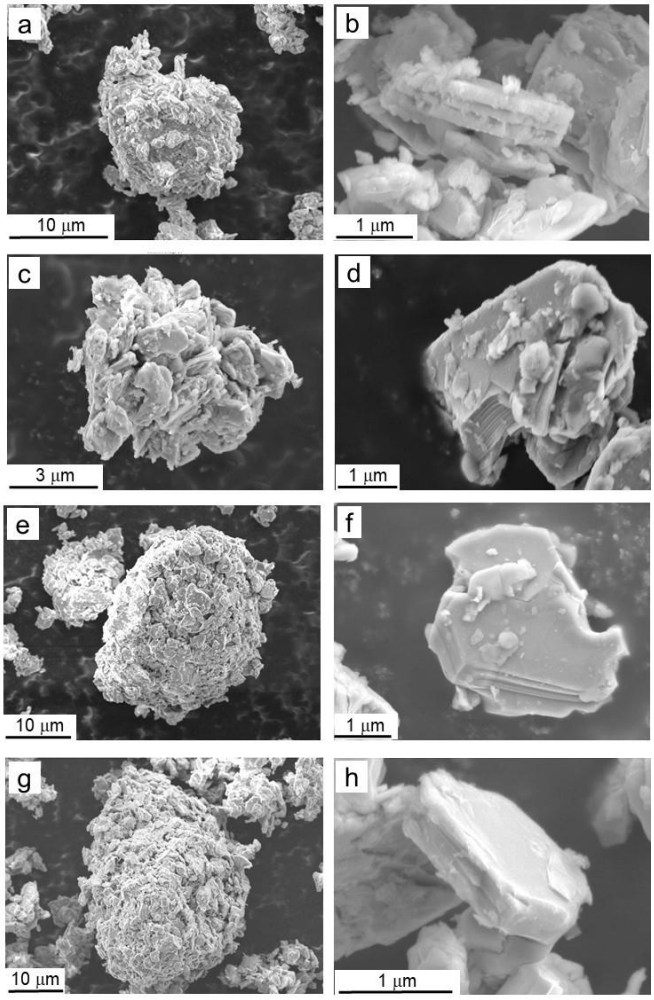

Figure 2. FE-SEM micrographs of a, b) NMFN0; c, d) NMFN05; e, f) NMFN10 and g, h) NMFN15 at two different magnifications.

FE-SEM micrographs, displayed in Figure 2, show the most relevant morphological properties at two different magnifications. On the one hand, primary particles are randomly agglomerated as rounded particles with a diameter of a few micrometers (Figures 2 a, c, e, and g). A close inspection of isolated primary particles evidences the parallel stacking of crystal stratus reflecting the layered structure of these oxides (Figures 2 b, d, f, and f). EDX analysis revealed a uniform distribution of the compositing elements on the particle surface, which demonstrates the reliability of the selected sol-gel route to yield homogenous phases (Figure S1, Supporting information).

In general, the HRTEM images in Figure 3 evidence the high crystallinity of the studied samples, as well as different orientations of the layered particles relative to the electron beam. Figures 3a and c show lattice fringes ascribable to the (002) planes of the NMFN0 and NMFN15 P2-stacking phases, which are separated by 5.61 and 5.64 Å, respectively. These values are in good agreement with the unit cell c dimensions collected in Table 1, which in turn indicate the cell expansion caused by nickel incorporation in the lattice. In addition, they show significant layer curvature due to internal stresses. On the other hand, <001> zone

axes could be identified in Figures 3b and d and their corresponding fast Fourier transform (FFT) plots. The images reveal a local disorder leading to different regions, as well as fringes ascribable to the (100) and (010) structure planes with spacings close to 2.50 Å. Also, images with a more extended field reveal a local disorder leading to different crystalline domains, particularly evident for sample NMFN15.

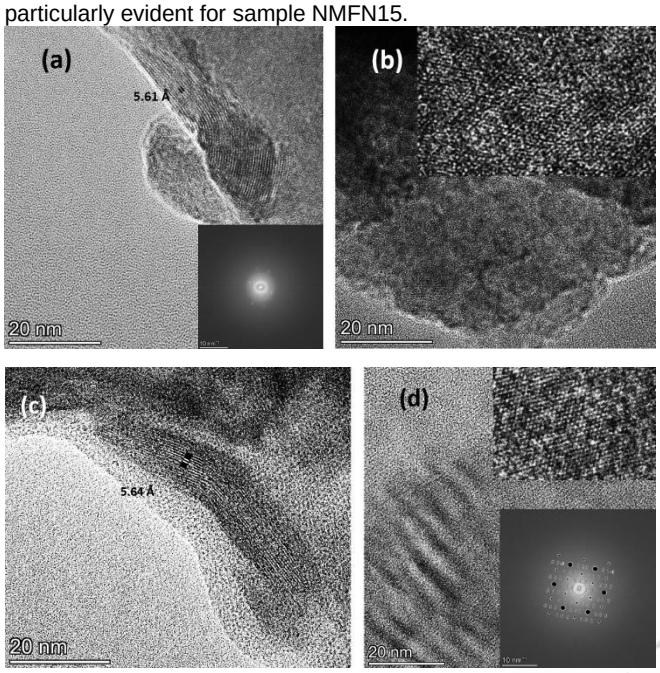

Figure 3. HRTEM images and electron diffraction diagrams of NMFN0 and NMFN15 samples.

Figure 4 shows the X-ray photoelectron spectra at the Mn2p, Fe2p, and O1s core levels of the NMFN0 raw sample and their corresponding counterparts in partially and fully charged electrodes. For the pristine material, the Fe2p profiles feature two characteristic bands at 711.0 eV and 724.6 eV which are respectively assigned to $Fe2p_{3/2}$ and $Fe2p_{1/2}$ levels of this transition metal in its trivalent state. The presence of a satellite peak at 717.6 eV is also remarkable.[37, 38] For the $Mn2p_{3/2}$ subspectra, the asymmetric band was decomvoluted in components at 642.0 eV and 643.0 eV ascribable Mn^{3+} and Mn^{4+}. In fact, a linear correlation between the average oxidation state (AOS) of manganese derived from the nominal stoichiometry and the relative contribution these XPS components was observed (Figure S2, Supporting information). Finally, The O1s spectrum shows an asymmetric profile that can be decomposed into three components at 529.5 eV, 530.8 eV, and 533.6 eV coming from the lattice oxide species and surface carbonated species.[39] Additionally, spectra at the Na1s, Mg1s, and Ni2p were also recorded for the studied samples (Figures S3-S6, Supporting information). The binding energies associated with the maxima of their bands were in good agreement with the presence of Na^+, Mg^{2+}, and Ni^{2+}, respectively.[40, 41] A significant contribution of Ni^{3+} (856.7 eV), due to oxidative conditions at the particle surface, could be responsible for the asymmetric Ni2p.[42]

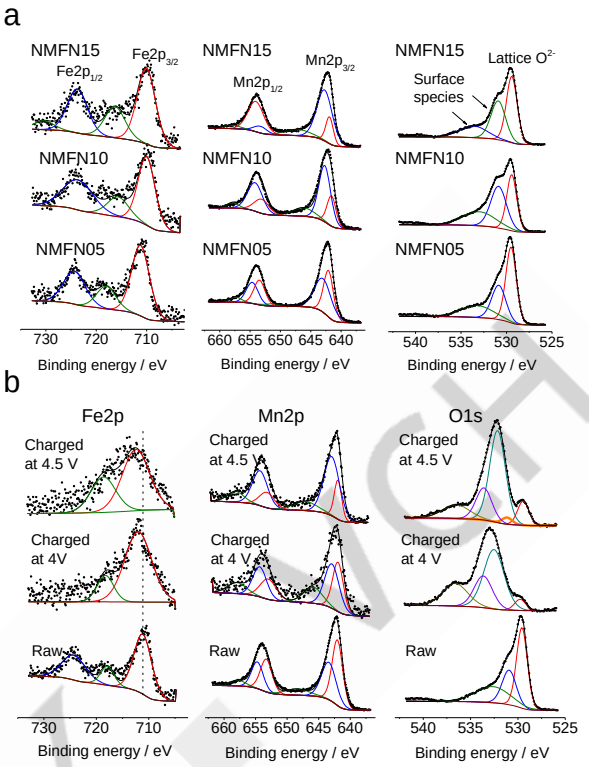

Figure 4. XPS spectra at the Mn2p, Fe2p, and O1s core levels of a) NMFM05, NMFN10 and NMFN15 raw samples; b) NMFN0 raw sample and electrodes charged at 4.0 and 4.5 V.

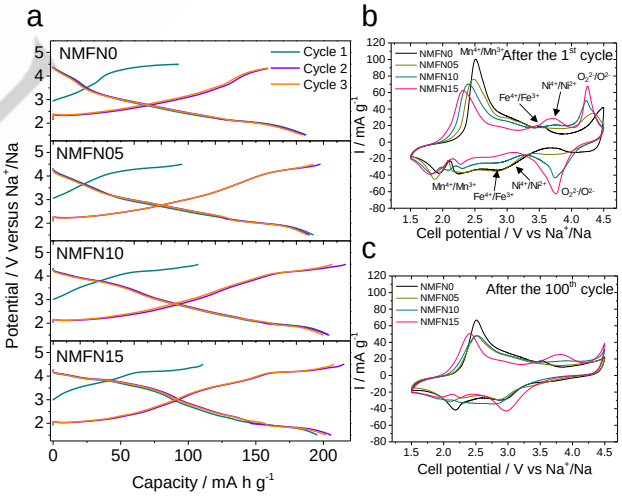

Figure 5. a) First three galvanostatic cycles recorded between 1.5 and 4.5 V at C/10 and room temperature; Cyclic voltammograms for the $Na_{0.67}Mg_{0.05}Fe_{0.1}Ni_xMn_{0.85-x}O_2$ ($0 \le x \le 0.15$) samples b) recorded at 0.1 mV s^{-1} and c) after the first cycle at C/10 (18 mA g^{-1}) and c) 100th cycle at 1C.

Figure 5a shows the first three galvanostatic cycles at C/10 to unveil a first short charge whose extent increases with the Ni content. Also, an increase in the capacity of the first discharge is observed when the Ni content is increased. Likely, the capability of this transition metal of transferring two electrons according to the Ni^{4+}/Ni^{2+} redox couple as compared to Fe^{4+}/Fe^{3+} or Mn^{4+}/Mn^{3+} couples can be responsible for this slightly high capacity at low

10.1002/cssc.202301327

rates. To allocate the redox activity of these redox couples and correlate them to the stoichiometry of the studied compounds, CV curves at a low sweep rate (0.1 mV s^{-1}) were scanned (Figure 5b). The anodic profiles reveal distinct features at ca. 2.5, 3.3, and 3.7, which are respectively ascribed to the Mn^{4+}/Mn^{3+}, Fe^{4+}/Fe^{3+}, Ni^{4+}/Ni^{2+}. Their changes of intensity are in good agreement with the nominal stoichiometry of samples. The fourth band at ca. 4.2 V is visible for those samples with high Ni content, while is shifted to higher voltages for samples NMFN0 and NMFN05. Either a P2 transition phase to an irreversible O2 phase or the oxidation of oxide anions to peroxo species are proposed.[21, 43] This high voltage band was reversible for the first few cycle at low rates (Figure 5a). The fact that this band appears over the upper cut-off voltage NMFN0 and NMFN05 may explain their slightly lower capacity in the subsequent discharge (Figure 5a). All these anodic bands showed their corresponding cathodic counterparts, as indicated in Figure 5b. After the 100th cycle at 1C, these voltammograms revealed the disappearance of the bands at ca. 4.2 V (Figure 5c), while those bands assigned to the oxidation and reduction of the transition metals were still visible. Therefore, it is plausible that the influence of this high voltage process on the long cycling performance would be limited to the first few cycles and even to be responsible for limited sodium diffusion at high rates as will be shown below. Recently, Du et al. have found that Na^+ removal from a related layered oxide also reveals a flat plateau at ca. 4.2 V, ascribable to the introduction of holes into the O-2p bands. Nevertheless, the limited reversibility of the O-2p band oxidation lead to a capacity fade of this plateau on cycling.[44]

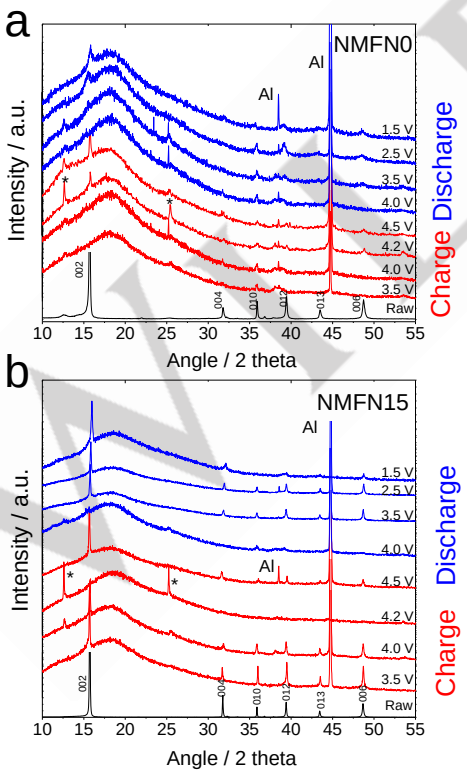

Figure 6. Ex-situ XRD patterns of raw material, electrodes charged at 4.2 and 4.5 V and subsequent discharged at 1.5 V for a) NMFN0 and NMFN15 samples. Asterisks denotes the reflections ascribable to the electrolyte inserted phase.

The nature of the process involved in the high voltage bands could be discerned with the help of ex-situ XRD and XPS techniques. Figure 6 shows the ex-situ XRD patterns of partially charged electrodes for two selected samples. New peaks at 12.6º and 25.2ºare predominant at 4.2 V. These reflections are typically attributed to the cointercalation of solvent molecules into the sodium slabs.[45] Further charge at 4.5 V involved the disappearance of this solvated phase and the reappearance of the P2 phase evidencing the reversibility of this process. Li et al. revealed that the contribution to the reversible capacity in the Na/P3-$Na_{0.5}Ni_{0.25}Mn_{0.75}O_2$ at high voltage arose from the combined contribution of the reversible insertion of the electrolyte anions (v.g.:ClO_4^-) and the anionic activity (O_2^{2-}/O^{2-}) redox couple, resulting in a fast-kinetics process.[46] A partially crystalline P2 phase is recovered after further discharge at 1.5 V. At this low voltage, the reduction to Mn^{3+} may induce a significant Jahn-Teller effect which elongates the octahedral sites and provokes structural degradation on cycling.[47] This effect involves the splitting of the (002) and (004) reflections due to the appearance of a P2' phase.[48] The absence of these split signals in the patterns of the discharged electrodes (Figure 6) would reveal that this deleterious phenomenon is circumvented in these samples. In this way, it has been reported that the substitution of Fe^{3+} by Mn^{4+} and or Ni^{2+} allows to mitigate this undesired effect.[49]

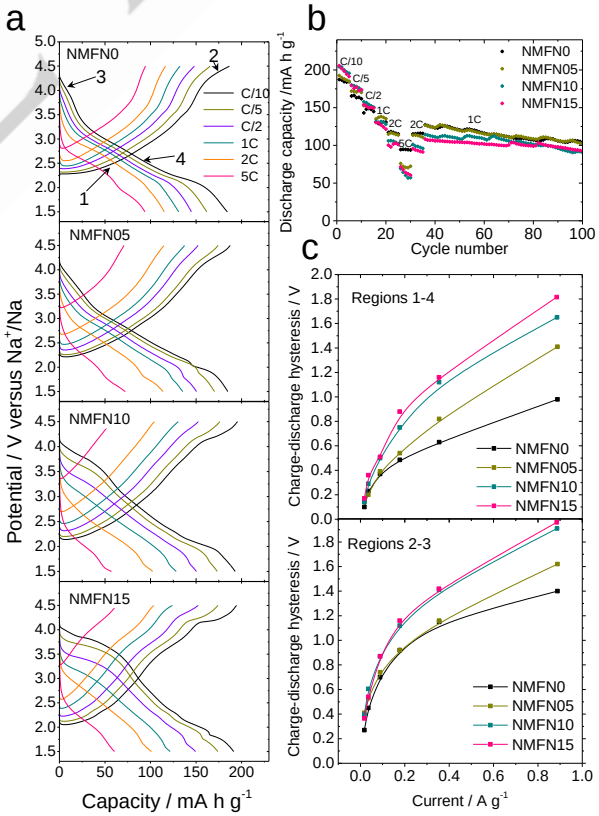

Figure 7. a) Galvanostatic charge-discharge branches of sodium half-cells subjected to increasing rates from C/10 to 5C; b) Rate capability of half-cells cycled between 1.5 and 4.5 V at several

rates from C/10 to 5C; c) Charge-discharge hysteresis versus applied current measured at the low voltage (1-4) and high voltage (2-3) regions. These regions have been indicated with arrows in Figure 7a.

To unveil the participation of elements in the electrochemical reaction, XPS spectra of charged electrodes were recorded for the NMFN0 sample (Figure 4b). After cell charging, the fitted Mn2p revealed an increase of the band assigned to Mn^{4+}, as expected from the electrochemical oxidation induced during the charging process. Similarly, a slight shift of the $Fe2p_{3/2}$ band to high binding energies would involve the presence of an non-resolved component of tetravalent iron after the cell charging.[38] Concerning the O1s spectra, the electrochemical oxidation induced an increase of the contribution of component attributed at surface adsorbed species. Also, a small component at 531.4 eV, which has been ascribed to the presence of electrochemically oxidized peroxo species, could be observed after charging at 4.5 V.[39, 43, 50]

Sodium half-cells assembled with the studied samples as working electrodes were subjected to rate capability tests at rates from C/10 to 5C, then 2C, and finally 1C until the 100th cycle. Charge and discharge branches are plotted in Figure 7a to unveil different behaviors at both capacity values and average voltage at charge and discharge that have been separately evaluated. First, overall discharge capacity values have been calculated and displayed in Figure 7b. It seems clear that the contribution of the extra capacity due to the P2 transition phase and/or anionic redox activity at high cell voltage is beneficial for NMFN10 (204 mA h g^{-1}) and NMFN15 (206 mA h g^{-1}) after the first discharge at C/10. Their comparatively high capacity persisted until the C/2 rate. Then, an enhanced capacity fading is recorded for the latter samples at the highest rates from 1C to 5C. Thus, discharge capacity values as low as 57 mA h g^{-1} and 60 mA h g^{-1} were respectively recorded for NMFN10 and NMFN15. It can be attributed to the poor reversibility of the plateau at 4.2 V when the cell is subjected to high currents, but also to the increase of the charge and discharge hysteresis occurring when the Ni content is increased. (Figure 7a). Contrarily, the low voltage region between 3 and 4 V during charge, and 1.5 and 2.5 V during discharge, mainly due to the Mn^{4+}/Mn^{3+} redox couple appears less polarized and able to sustain capacity at high rates. Contrarily, the Ni-free NMFN0 sample featured 131, 115, and 94 mA h g^{-1}.at 1C, 2C and 5C. Besides the environmental benefits of the removal of nickel from its composition, these values are highly competitive to others previously reported in the literature, mainly at the highest kinetic rate. (Table S1; Supporting information). Concerning the capacity retention during the cycling at 1 C, values of 81.4%, 80.7%, 79.2%, and 85.6% were respectively determined for NMFN0, NMFN05, NMFN10, and NMFN15.

To clarify this effect, two distinct regions were discerned in both charge (1-2) and discharge (3-4) curves at high and low voltages, which have been marked in Figure 7a. Their average voltage was determined and the charge-discharge hysteresis was plotted versus the mass normalized current in Figure 7c. The hysteresis followed a non-linear variation. The tendency revealed that the presence of nickel favors large cell polarization that eventually negatively affects the overall discharge capacity. It agrees with the rate capability results, demonstrating that nickel can be fully removed from the electrode composition benefiting at the same time exceptional performance at high rates.

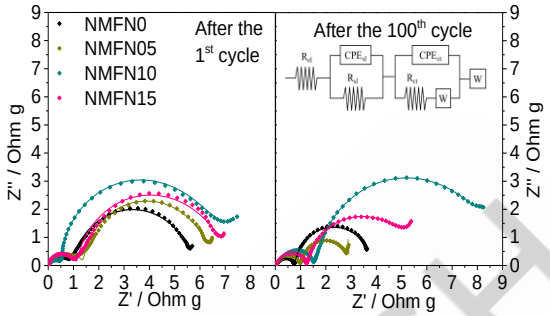

Figure 8. a) Nyquist plots for the $Na_{0.67}Mg_{0.05}Fe_{0.1}Ni_xMn_{0.85-x}O_2$ ($0 \le x \le 0.15$) samples recorded after the first cycle at C/10 and the 100th cycle at 1C. Inset: Equivalent circuit used for the fitting of the spectra.

To unveil the effect of the resistance at the electrode-electrolyte interphase on the cell performance, impedance spectra were recorded after the first discharge at C/10 and the 100th cycle at 1C. Figure 8 shows the Nyquist plots whose profiles feature typical semicircles at high and low frequencies. From their fitting to the equivalent circuit appearing as an inset in this figure, internal resistances at the electrolyte (R_{el}), the surface layer (R_{sl}), and charge-transfer reaction (R_{ct}) at the electrode/electrolyte interphase can be determined (Table 3). R_{el} yielded values that can be neglected as compared to the others, as expected for electrolytes in solution. After the first cycle, the lowest resistance values were recorded for NMFM0 and NMFN05 samples. After the 100th cycle, the overall cell resistance decreased for all samples except for NMFN10. These results evidence the good kinetic response of those samples with low Ni contents and the flexibility of their open framework to favor Na migration even after a large number of cycles. The lowest resistance performed by NMFN05 after 100 cycles could be correlated to its ability to retrieve cell capacity when returning to 2C and then 1C. and eventually reaching capacity values close to those of NMFN0 after the 100th cycle.

Table 3 Electrolyte (R_{el}), surface layer (R_{sl}) and charge transfer (R_{ct}) resistance values. calculated from the impedance spectra of the studied Mg-doped studied samples after 1st cycle at C/10 and 100 cycles at different 1C rates.

	NMFN0	NMFN05	NMFN10	NMFN15
After 1st cycle at C/10				
R_{el} / Ohm g	0.004	0.002	0.001	0.002
R_{sl} / Ohm g	1.002	1.436	0.561	1.13
R_{ct} / Ohm g	5.198	4.968	6.328	5.62
After 100th cycle at 1C				
R_{el} / Ohm g	0.023	0.013	0.018	0.019

R_{sl} / Ohm g	0.746	1.005	1.597	1.228
R_{ct} / Ohm g	3.015	1.856	6.782	3.932

Cyclic voltammetry at increasing sweep rates was applied to the sodium half-cells previously subjected to one charge and discharge activation cycle at C/10 (Figure S7a; Supporting information). From these curves, the relative faradaic and capacitive contributions can be calculated. The faradic one arises from the Na^+ insertion and the electron transfer at the redox-active sites. Otherwise, the strong electrostatic interactions among the metal oxide slabs that eventually lead to the Na^+ release from the structure are considered the origin of the capacitive response.[51] For this purpose, current values at the selected peak maxima (I_p) along the anodic (1-2) and their corresponding cathodic counterparts (3-4) were measured. They are marked in Figure S7a. These values follow a linear relationship versus the sweep rate ν according to the next equation:[52]

$$\log I_p = \log a + b \log v \qquad \text{[Eq.1]}$$

From the slope, b-values can be elucidated (Figure S8; Supporting information). This parameter takes values between 0.5 and 1, being 0.5 ascribable to a faradic diffusion-limited reaction, b-values close to 1.0 are typical of predominantly capacitive response. The lower activation barriers associated with the electrostatic interactions linked to the capacitive process may positively contribute to a fast exchange of Na^+. Figure 9a shows a predominant faradic contribution except for NMFN0 which revealed the highest b- values, mainly for the high voltage peaks 2 and 3.

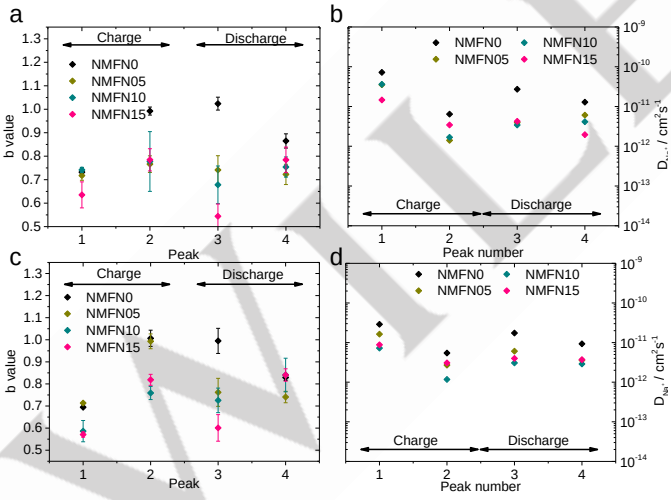

Figure 9. Plot of b-values for the $Na_{0.67}Mg_{0.05}Fe_{0.1}Ni_xMn_{0.85-x}O_2$ ($0 \le x \le 0.15$) samples recorded a) after the first cycle at C/10 and c) the 100th cycle at 1C. Plots of apparent diffusion coefficients recorded b) after the first cycle at C/10 and d) the 100th cycle at 1C.

Apparent sodium diffusion coefficients (D_{Na^+}) can also be calculated from the CV curves in Figure S7a. It is well known the linear relationship existing between the current intensity maxima (I_p) and the square root of the sweep rate (Figure S9; Supporting information):[53]

$$I_p = 2.69\times10^{-5} n^{3/2} S D_{Na^+}{}^{1/2} C v^{1/2} \qquad \text{[Eq.2]}$$

Equation 2 also features S as the geometric electrode area, n is the number of transferred electrons and C is the Na^+ concentration. The diffusion coefficients (D_{Na^+}), displayed in Figure 9b, took values between 1.10^{-10} and 1.10^{-12} cm^2s^{-1}, the highest values belonging to NMFN0 irrespective of the current peak. These results pointed out a good kinetic behavior of the latter sample and would justify its exceptional performance on cycling at rates as high as 5C.

GITT experiments were alternatively performed to calculate sodium diffusion coefficients (Figure S10 (supporting information)). As expected, these pulse-relaxation curves feature similar profiles to those displayed in Fig. 6a at the lowest rate. This chrono-potentiometric technique is performed by applying a series of constant current pulses (C/10) for a limited transient time (τ=30 min) that increase the Na content in a certain Δx, followed by a relaxation time (60 min) (Figure S11a (supporting information)). The sodium diffusion coefficient can be calculated whether a linear relationship between the cell voltage versus the square root of the transient time is followed (Figure S11b (supporting information)). For this purpose, the next equation is applied:[54]

$$D_{Na^+} = \frac{4}{\pi\tau}\left(\frac{m V_M}{M A}\right)^2 \left(\frac{\Delta E_s}{\Delta E_\tau}\right)^2 \qquad \text{[Eq.3]}$$

In this expression, τ is the transient time, *m is* the active material mass, *M* is the molar mass, V_M is the molar volume, and *A* is the electrode surface. Otherwise, ΔE_s and ΔE_t, are measurable parameters from the GITT curves as depicted in Figure S11a. The sodium diffusion coefficients are plotted in Figure S12 (supporting information) as a function of the cell capacity in both charge and discharge. Irrespective of the sample, a common S-shape profile can be discerned. The coefficients decrease at the beginning of the sweep to be further slightly increased during the central region of the curve corresponding to the intermediate content of sodium into the host matrix. This trend is confirmed by the coefficients calculated from the CV curves and the Randles-Sevcik equation which are plotted in Figure 9b. The sodium exhaustion or full occupation from vacant sites leads to an abrupt decrease of coefficients at the charge and discharge branches, respectively. The average calculated values at mid-term charge capacity were quite similar among samples ($1.8\ 10^{-10}$ $cm^2\ s^{-1}$), while slightly higher values were recorded for NMFN0 ($3.4\ 10^{-10}$ $cm^2\ s^{-1}$) than for the other samples nickel-containing samples ($1.8\ 10^{-10}$ $cm^2\ s^{-1}$). These values are close to those calculated from the voltammograms and equation 2, confirming their validity.

A similar kinetic study was performed on the sodium half-cell retrieved after the 100th cycle at 1C to correlate their capacity degradation after the cycling experiment to their kinetic properties. Figure S7b (Supporting information) shows CV curves recorded at increasing sweep rates which were employed to determine the current intensity maxima (I_p). The overall anodic and cathodic profiles resemble those recorded after the first cycle, though their current intensity has decreased as a result of the capacity fading. Also, the bands at high voltage, associated with the P2 phase transition, have disappeared as a consequence of the poor reversibility of this process. The b-values were also calculated from the linear relationship between log *I* and log ν (Figure S13,

10.1002/cssc.202301327

Supporting information). In general terms, only small variations can be appreciated in these values after cycling. The high capacitive contribution in NMFN0, mainly at peaks 2 and 3 is preserved upon cycling (Figure 9c). Concerning apparent diffusion coefficients, the Randles-Sevcik method was applied according to Equation 2 (Figure S14, Supporting information). The results revealed also small changes as compared to Figure 9d. It evidences the good structural stability of these layered oxides which allows for the preservation of the Na^+ diffusion path even after a long number of cycles.

Eventually, sodium half-cells assembled with the NMFN0 sample were subjected to galvanostatic cycling at different conditions (Figure 10). On the one hand, the capability of future batteries to sustain continuous cycling at low temperatures is highly demanding. Figure 10a evidences that our best-performing NMFN0 sample can retain 40 mA h g^{-1} (1C) after 200 cycles at temperatures as low as -15ºC. Otherwise, a cycling experiment at a 2C rate and room temperature yielded 75 mA h g^{-1} and an excellent coulombic efficiency (Figure 10b).

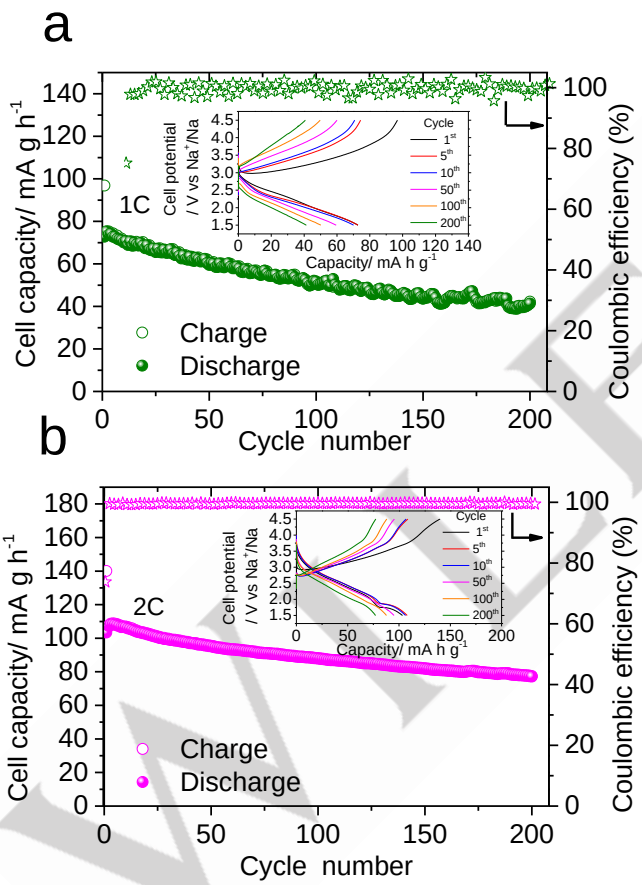

Figure 10: Galvanostatic cycling of sodium half cells assembled with NMFN0 sample as the working electrode. a) -15ºC and 1c rate; b) room temperature and 2C rate.

Conclusion

On searching for new electrode compositions as positive electrodes for sodium-ion batteries, limiting their Ni contents, the $Na_{0.67}Mg_{0.05}Fe_{0.1}Ni_xMn_{0.85-x}O_2$ (x= 0.0, 0.05, 0.1, 0.15) series has been studied in this work. The sol-gel route ensures a low-cost and easily scalable preparative procedure. The structural, morphological, and compositional evaluation of raw samples was carried out by solid-state techniques such as X-ray diffraction, electron microscopy, and X-ray fluorescence, respectively. These results revealed highly pure and crystalline samples, indexable in the layered P2 type structure, and a good accordance between the nominal and actual compositions. XPS spectroscopy of raw samples confirmed the expected valence states for iron and manganese, respectively.

The rate capability tests, performed on half-sodium cells assembled with the prepared electrodes, evidenced an exceptional performance for the Ni-free sample (NMFN0), even at the highest rate (94 mA h g^{-1}). XRD and XPS ex-situ measurements revealed the combined participation of the reversible electrolyte insertion and peroxo species formation. The high reliability of this electrode material has been explained in terms of a good kinetic response resulting in a low hysteresis between the charge and discharge branches, high Na^+ diffusivity, and low cell resistance. These excellent properties were preserved after 100 cycles and it was responsible for the remarkable electrochemical behavior when this electrode material was cycled either to low temperatures or high rates.

Experimental section

Four samples with general composition $Na_{0.67}Mg_{0.05}Fe_{0.1}Ni_xMn_{0.85-x}O_2$ (x= 0.0, 0.05, 0.1, 0.15) by an easy scalable sol-gel procedure. The Mg content was eventually chosen according to the literature in which moderate substitutions were enough to evidence the positive effect on the cathode performance.[22] The sol-gel synthesis resided on the use of citric acid (Aldrich, 99%) as a chelating agent in a 3 to 2, citric to metal ratio. Thus, stoichiometric amounts of $Ni(NO_3)_2.6H_2O$ (Aldrich, 99%), $Mn(NO_3)_2.4H_2O$ (Aldrich, 99%), iron nitrate nonahydrate $Fe(NO_3)_3{\cdot}9H_2O$ (Aldrich, 99%) and magnesium nitrate hexahydrate $Mg(NO_3)_2.6H_2O$ (Aldrich, 98% purity) were dissolved in 50 mL containing the citric acid solution. Finally, sodium acetate (Aldrich, 99%) was added in a 5% excess to counterbalance losses upon calcination. The samples will be named NMFN0, NMFN05, NMFN10, and NMFN15, for x values equivalent to 0, 0.05, 0.1, and 0.15, respectively.

A BrukerD8 Discover A25 diffractometer, furnished with Cu-*K*α radiation and a graphite monochromator, was used to determine the crystallinity and purity of the studied samples. For this purpose, the X-ray diffraction patterns were recorded from 10 to 90º (2θ) (step size: 0.04° for 672 s) to evidence the purity and crystallinity of samples. *TOPAS* software allowed for calculating the lattice parameters. X-ray photoelectron emission spectroscopy (XPS) on raw and cycled materials was performed in a *SPECS Phobios 150 MCD* XPS spectrometer, furnishing an Al *K*α source. Samples were previously outgassed at a high vacuum overnight. The binding energy was calibrated from the C1s line of the adventitious carbon (284.6 eV). A JSM-7800F Prime JEOL Microscope, equipped with an EDX analyzer allowed

to record Field Emission-Scanning Electron micrographs (FE-SEM). High-Resolution Transmission Electron Microscopy (HRTEM) images were recorded in a TALOS F200i. A ZSX Primus IV Rigaku sequential wavelength dispersive spectrometer was used to analyze the X-ray fluorescence (XRF) and thus determine the elemental composition.

Working electrodes of the synthesized materials were prepared by mixing the active material (70%), acetylene black (20%), and PVDF (polyvinylidene fluoride) (10%) in N-methyl-2-pyrrolidone (Emplura, 99.5%). After two hours, the homogenous paste spread onto an aluminum current collector and vacuum dried at 120 ºC for several hours. The eventual working electrode loaded ca. 3 mg cm^{-2}. The auxiliary electrodes consisted of a metallic sodium disk (Panreac, 99.8%). A 1M $NaClO_4$ (Strem, >99%) in propylene carbonate (PC) solution (Sigma-Aldrich, 99.7%) containing 2% wt. of fluoroethylene carbonate (FEC) (Sigma-Aldrich, 99%) was used as an electrolyte. This ion-conducting solution was soaked into glass fiber disks (GF/A-Whatman). The Swagelok™-type sodium half-cells were assembled in an argon-filled MBraun glove box under controlled O_2 and H_2O traces. Both voltammetric and galvanostatic tests were developed to unveil the electrochemical behavior of the studied electrode materials.

Rate capability was tested at room temperature between C/10 and 5C within the potential window 1.5 – 4.5 V versus Na^+/Na. In addition, cycling tests at -15ºC at 1C were also carried out. Cyclic voltammograms (CV) were scanned from 0.1 to 1 mV s^{-1} within the same voltage limits. The galvanostatic intermittent titration technique (GITT) was used to record quasi-equilibrium curves. For this purpose, C/10 rate pulses were applied for 30 minutes. Then the cell was allowed to relax at open-circuit for 1 hour. A VMP multichannel system allowed us to monitor these electrochemical tests. The kinetic response at the electrode/electrolyte interphase was evaluated by Electrochemical Impedance Spectroscopy (EIS). An SP-150 Biologic potentiostat allowed to perturb the open circuit voltage by an AC signal of 5 mV and record the spectrum from 100 kHz to 2 mHz. Before the measurements, the cycled cells were allowed to reach a quasi-equilibrium state by relaxing under open circuit conditions for at least 24 hours.

Supporting Information

The authors have cited additional references within the Supporting Information.

Acknowledgements

Authors are grateful for the financial support from the PLEC2021-007779 research project funded by MCIN/AEI/10.13039/501100011033 and the European Union “NextGenerationEU”/PRTR, entitled “Innovative electrodes and electrolytes for a new generation of sodium-based batteries for stationary applications (NABASTAT)”, and Junta de Andalucía (group FQM288). We also thank SCAI (UCO Central Service for Research Support) and IQUEMA.

Keywords: Sodium-ion batteries • intercalations; layered compounds • magnesium • doping

[1] Y. Liu, X. Liu, T. Wang, L.-Z. Fan, L. Jiao, *Sustain. Energy Fuels* **2017**, *1*, 986-1006.

[2] A. Mauger, C.M. Julien, *Materials* **2020**, *13*, 3453.

[3] N. Tapia-Ruiz, A.R. Armstrong, H. Alptekin, M.A. Amores, H. Au, J. Barker, R. Boston, W.R. Brant, J.M. Brittain, Y. Chen, M. Chhowalla, Y.-S. Choi, S.I.R. Costa, M. Crespo Ribadeneyra, S.A. Cussen, E.J. Cussen, W.I.F. David, A. V Desai, S.A.M. Dickson, E.I. Eweka, J.D. Forero-Saboya, C.P. Grey, J.M. Griffin, P. Gross, X. Hua, J.T.S. Irvine, P. Johansson, M.O. Jones, M. Karlsmo, E. Kendrick, E. Kim, O. V Kolosov, Z. Li, S.F.L. Mertens, R. Mogensen, L. Monconduit, R.E. Morris, A.J. Naylor, S. Nikman, C.A. O'Keefe, D.M.C. Ould, R.G. Palgrave, P. Poizot, A. Ponrouch, S. Renault, E.M. Reynolds, A. Rudola, R. Sayers, D.O. Scanlon, S. Sen, V.R. Seymour, B. Silván, M.T. Sougrati, L. Stievano, G.S. Stone, C.I. Thomas, M.-M. Titirici, J. Tong, T.J. Wood, D.S. Wright, R. Younesi, *J. Phys: Energy.* **2021**, *3*, 031503.

[4] P. Greim, A.A. Solomon, C. Breyer, *Nat. Commun*. **2020**, *11*, 4570.

[5] C. Helbig, A.M. Bradshaw, L. Wietschel, A. Thorenz, A. Tuma, *J. Clean. Prod.* **2018**, *172*, 274–286.

[6] Nagmani, D. Pahari, P. Verma, S. Puravankara*, J. Energy Storage* **2022**, *56*, 105961.

[7] M.A. Muñoz-Márquez, D. Saurel, J.L. Gómez-Cámer, M. Casas-Cabanas, E. Castillo-Martínez, T. Rojo, *Adv. Energy Mater.* **2017**, *7*, 1700463.

[8] H.S. Hirsh, Y. Li, D.H.S. Tan, M. Zhang, E. Zhao, Y.S. Meng, *Adv. Energy Mater.* **2020**, *10*, 2001274.

[9] F. Wei, Q. Zhang, P. Zhang, W. Tian, K. Dai, L. Zhang, J. Mao, G. Shao, *J. Electrochem. Soc.* **2021**, *168*, 050524.

[10] C. Delmas, D. Carlier, M. Guignard, *Adv. Energy Mater*. **2021**, *11*, 2001201.

[11 S. Chong, L. Yuan, S. Qiao, M. Ma, T. Li, X. L. Huang, Q. Zhou, Y. Wang, W. Huang, *Sci. China Mater*. **2023**, *66*, 2641–2651.

[12] S. Chong, L. Yuan, S. Qiao, M. Ma, T. Li, X. L. Huang, Q. Zhou, Y. Wang, W. Huang, *ACS Appl. Mater. Interfaces* **2021**, *13*, 13158−13169.

[13 S. Chong, M. Ma, L. Yuan, S. Qiao, S. Dong, H. Liu, S. Dou, *Energy Environ. Mater*. 2022, 0, e12458.

[14] Y. Zhu, Q. Yao, R. Shao, C. Wang, W. Yan, J. Ma, D. Liu, Ji. Yang, Y. Qian, *Nano Lett.* **2022**, *22*, 7976−7983.

[15] T. Yuan, Y. Sun, S. Li, H. Che, Q. Zheng, Y. Ni, Y. Zhang, J. Zou, X. Zang, S.-H. Wei, Y. Pang, S. Xia, S. Zheng, L. Chen, Z.-F. Ma, Nano Res. **2023**, 16, 6890−6902.

[16] T. Yuan, S. Li, Y. Sun, J.-H. Wang, A.-J. Chen, Q. Zheng, Y. Zhang, L. Chen, G. Nam, H. Che, J. Yang, S. Zheng, Z.-F. Ma, M. Liu, ACS Nano **2022**, *16*, 18058−18070.

[17] J.M. Paulsen, C.L. Thomas, J.R. Dahn, *J. Electrochem. Soc*. **2000**, *147*, 861.

[18] N. Yabuuchi, K. Kubota, M. Dahbi, S. Komaba, *Chem. Rev*. **2014**, *114*, 11636–11682.

[19] X. Wu, S. Jin, Z. Zhang, L. Jiang, L. Mu, Y.-S. Hu, H. Li, X. Chen, M. Armand, L. Chen, X. Huang, *Sci. Adv.* **2015**, *1*.

[20] I. Hasa, S. Passerini, J. Hassoun, *J. Mater. Chem. A*. **2017**, *5*, 4467–4477.

[21] Z. Lu, J.R. Dahn, *J. Electrochem. Soc.* **2001**, *148*, A1225.

[22] G. Singh, N. Tapia-Ruiz, J.M. Lopez del Amo, U. Maitra, J.W. Somerville, A.R. Armstrong, J. Martinez de Ilarduya, T. Rojo, P.G. Bruce, *Chem. Mater*. **2016**, *28*, 5087–5094.

[23] S. Su, X. Bai, L. Ming, Z. Xiao, C. Wang, B. Zhang, L. Cheng, X. Ou, *J. Solid State Chem*. **2022**, *308*, 122916.

[24] M. Bomio, P. Lavela, R.L. Tranquilin, F.V. da Motta, J.L. Tirado, *J. Electroanal. Chem.* **2023**, *930*, 117157.

[25] N. Campagnol, K. Hoffman, A. Lala, O. Ramsbottom, "The future of nickel: A class act" , can be found under https://www.mckinsey.com/industries/metals-and-mining/our-insights/the-future-of-nickel-a-class-act, **2017**. (Accessed: 09/04/2023).

[26] D. Darbar, T. Malkowski, E.C. Self, I. Bhattacharya, M.V.V. Reddy, J. Nanda, *Mater. Today Energy* **2022**, *30*, 101173.

[27] X. Zeng, M. Xu, J. Li, *Resour. Conserv. Recycl*. **2018**, *139*, 188–193.

[28] S. Bobba, I. Bianco, U. Eynard, S. Carrara, F. Mathieux, G.A. Blengini, *Energies* (Basel) **2020**, *13*, 2513.

[29] S. Chu, Y. Zhong, K. Liao, Z. Shao, *Curr. Opin. Green Sustain. Chem*. **2019**, *17*, 29–34.

[30] J. Yang, A.E. Maughan, G. Teeter, B.J. Tremolet de Villers, S. Bak, S. Han, *ChemSusChem* **2020**, *13*, 5972–5982.

[31] D. Zhou, W. Huang, X. Lv, F. Zhao, *J. Power Sources* **2019**, *421*, 147–155.

[32] J. Zhang, W. Wang, W. Wang, S. Wang, B. Li, *ACS Appl. Mater. Interfaces* **2019**, *11*, 22051–22066.

[33] R. Fielden, M.N. Obrovac, *J. Electrochem. Soc*. **2015**, *162*, A453–A459.

[34] C. Delmas, C. Fouassier, P. Hagenmuller, *Phys. B + C* **1980**, *99*, 81-85.

[35] C. Delmas, J.-J. Braconnier, C. Fouassier, P. Hagenmuller, *Solid State Ion*. **1981**, 3-*4*, 165-169.

[36] D. Buchholz, L.G. Chagas, C. Vaalma, L. Wu, S. Passerini, *J. Mater. Chem. A*. **2014**, *2*, 13415–13421.

[37] D. Zhou, C. Zeng, D. Ling, T. Wang, Z. Gao, J. Li, L. Tian, Y. Wang, W. Huang, *J. Alloys Compd.* **2023**, *931*, 167567.

[38] D. Yuan, X. Hu, J. Qian, F. Pei, F. Wu, R. Mao, X. Ai, H. Yang, Y. Cao, *Electrochim. Acta.* **2014**, *116*, 300–305.

[39] D.P. Siriwardena, J.F.S. Fernando, T. Wang, K.L. Firestein, C. Zhang, C. Lewis, J.E. Treifeldt, D. V. Golberg, *ChemElectroChem*. **2021**, *8*, 508–516.

[40] K. Tang, Y. Huang, X. Xie, S. Cao, L. Liu, M. Liu, Y. Huang, B. Chang, Z. Luo, X. Wang, *Chem. Eng. J.* **2020**, *384*, 123234.

[41] S. Su, X. Bai, L. Ming, Z. Xiao, C. Wang, B. Zhang, L. Cheng, X. Ou, *J. Solid State Chem.* **2022**, *308*, 122916.

[42] K.M. Shaju, K. V. Ramanujachary, S.E. Lofland, G. V. Subba Rao, B.V.R. Chowdari, *J. Mater. Chem*. **2003**, *13*, 2633.

[43] M. Jia, Y. Qiao, X. Li, F. Qiu, X. Cao, P. He, H. Zhou, *ACS Appl. Mater. Interfaces* **2020**, *12*, 851–857.

[44] K. Du, J. Zhu, G. Hu, H. Gao, Y. Li, J. B. Goodenough, *Energy Environ. Sci*. **2016**, *9*, 2575-2577.

[45] P. Hou, Y. Sun, F. Li, Y. Sun, X. Deng, H. Zhang, X. Xu, L. Zhang, *Nanoscale* **2019**, *11*, 2787-2794.

[46] Q. Li, Y. Qiao, S. Guo, K. Jiang, Q. Li, J. Wu , H. Zhou, *Joule* **2018**, *2*, 1–12.

[47] S. Kumakura, Y. Tahara, K. Kubota, K. Chihara, S. Komaba, *Angew. Chem., Int. Ed.* **2016**, *128*, 12952-12763.

[48] B. Mortemard de Boisse, D. Carlier, M. Guignard, L. Bourgeois, C. Delmas, *Inorg. Chem*. **2014**, *53*, 11197-11205.

[49] E. Talaie, V. Duffort, H. L. Smith, B. Fultz, L. F. Nazar, *Energy Environ. Sci.* **2015**, *8*, 2512-2523.

[50] X. Bai, M. Sathiya, B. Mendoza-Sánchez, A. Iadecola, J. Vergnet, R. Dedryvère, M. Saubanère, A. M. Abakumov, P. Rozier, J.-M. Tarascon, *Adv. Energy Mater*. **2018**, *8*, 1802379.

[51] M. Valvo, S. Doubaji, I. Saadoune, K. Edström, *Electrochim. Acta*. **2018**, *276*, 142–152.

[52] T. Brezesinski, J. Wang, J. Polleux, B. Dunn, S.H. Tolbert, *J. Am. Chem. Soc*. **2009**, *131*, 1802–1809.

[53] J.E.B. Randles, *Trans. Faraday Soc*. **1948**, *44*, 327–338.

[54] X.H. Rui, N. Ding, J. Liu, C. Li, C.H. Chen, *Electrochim. Acta* **2010**, *55*, 2384–2390.

10.1002/cssc.202301327

WILEY VCH

RESEARCH ARTICLE

Entry for the Table of Contents

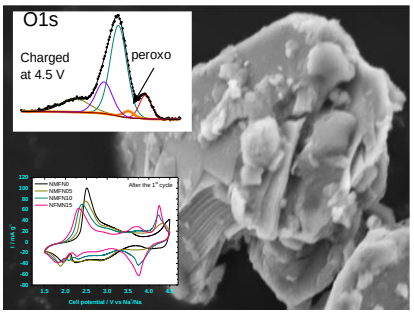

New P2 type $Na_{0.67}Mg_{0.05}Fe_{0.1}Ni_xMn_{0.85-x}O_2$ (x= 0.0, 0.05, 0.1, 0.15) electrodes are characterized as cathodes in sodium-ion batteries. Ni-free sample reveal a superior performance, which is associated to the combined contribution of reversible electrolyte insertion and formation of peroxo species. It evidences a low cycle hysteresis, high Na^+ diffusivity, and low cell resistance.